Transportation Engineering 2 (2020) 100027

Contents lists available at ScienceDirect

Transportation Engineering

journal homepage: www.elsevier.com/locate/treng

Computational study of ECN Spray A and Spray D combustion at different ambient temperature conditions

J.M. García-Oliver, R. Novella, J.M. Pastor*, L. Pachano

CMT-Motores Térmicos, Universitat Politècnica de València, Spain

A B S T R A C T

The combustion process of the Engine Combustion Network (ECN) Spray A and Spray D is studied over a wide range of ambient temperatures from 750 K to 900 K. With nominal diameters of 89.4 μm for the Spray A and 190.3 μm for the Spray D, these n-dodecane sprays are representative for light- and heavy-duty compression ignition engine applications, respectively. Computational Fluid Dynamics calculations are carried out using a Lagrangian parcel Eulerian fluid approach in a Reynolds averaged Navier–Stokes framework. For the Spray D reference condition, two sub-grid flame structure assumptions and the effect of turbulence chemistry interaction (TCI) on autoignition and flame structure at quasi-steady state are assessed in the context of a well-mixed and an Unsteady Flamelet Progress Variable (UFPV) combustion model. After that, UFPV approach is used to evaluate combustion behavior for the different ambient temperature conditions. Reference condition results show that both well-mixed and flamelet assumptions lead to a similar autoignition sequence. In terms of ignition delay time, TCI plays an important role, within the UFPV model, in reproducing the experimental trend observed for the increase in nozzle diameter. In terms of lift-off length, the well-mixed model is observed to predict a longer value compared to the flamelet-based sub-grid assumption. Lastly, the analysis of the autoignition sequence and flame structure at quasi-steady state is also extended over the whole range of ambient temperature conditions.

1. Introduction

Since its origin, the Engine Combustion Network (ECN) [1] has focused on the improvement of the state-of-the-art knowledge on the most relevant physical and chemical aspects of combustion processes by combining advanced experimental and modeling techniques. The end goal has been the development of highly predictive Computational Fluid Dynamic (CFD) models that enable an improved design of current and future powertrains for transport applications. One of the core ECN working groups focuses its activities on the fundamental analysis of transient two-phase inert and reacting Diesel-like sprays that mimic as much as possible the combustion system characteristic of current and future Compression-Ignition (CI) engines.

Initially, ECN efforts concentrated on the Spray A setup targeting the combustion system of High-Speed Direct Injection (HSDI) CI engines. An extensive Spray A experimental database containing detailed information generated through different parametric studies is already available, including liquid and vapor penetrations under inert and reacting conditions [2,3], mixing (mixture fraction) fields under inert conditions [4], ignition delay and lift-off length [5,6] or spatial distribution of key combustion species [7] and soot emissions [8,9]. More recently, two larger hole nozzles, namely Spray C and Spray D, targeting the combustion system of Heavy-Duty (HD) CI engines have also received attention in terms of detailed experiments with similar combustion metrics available [6,10,11].

In parallel, significant Spray A, Spray C and Spray D CFD modeling activities are being also carried out with the aim of complementing the insight provided by the experiments by accessing information otherwise not available with the current experimental techniques. However, the modeling setups found in the literature are quite heterogeneous and several combinations of turbulence and turbulence-chemistry interaction (TCI) models have been evaluated. Thus, the different attempts include well-mixed (WM) [12–16] and flamelet-based [17–23] combustion models in both Reynolds Averaged Navier–Stokes (RANS) and Large Eddy Simulation (LES) turbulence modeling frameworks, together with Conditional Moment Closure (CMC) [24] and Lagrangian Transported Probability Density functions (TPDF) combustion models [25,26] only in the RANS turbulence modeling environment. In the literature, some works have been carried out to assess the effect of TCI while keeping the chemical mechanism and the rest of the computational setup unchanged. In particular there are several works focused on this type of study in turbulent sprays comparing WM models and TPDF [27,28] models and an Eulerian Stochastic Field Probability Density function (ESF-PDF) model [29]. In this regard, there are also several works comparing WM models with flamelet-based models in turbulent sprays [22,30,31] and CI engines [22,32]. Despite the fact that these models provide encouraging results, particularly in terms of ignition delay and lift-off length macro-parameters predictions, there is still no evident superiority of none of them over the others. In fact, there is not a clear trend when comparing WM results with those of models accounting for TCI. In turbulent spray flame applications, the trends reported heavily depend on the boundary conditions under study. In general terms, at high-density conditions ($\sim$ 30 kg/m^3) ignition delay results for WM models compared to TPDF [27] and ESF-PDF [29] models are virtually the same for different ambient oxygen concentrations. At lower density conditions

* Corresponding author.
E-mail address: jopasen@mot.upv.es (J.M. Pastor).

https://doi.org/10.1016/j.treng.2020.100027
Received 1 July 2020; Received in revised form 24 August 2020; Accepted 3 October 2020

Table 1
Target sprays injection and thermodynamic boundary conditions.

Injection conditions	
Fuel	n-dodecane
Nozzle	89.4 μm – Spray A
diameter	190.3 μm – Spray D
Injection pressure	150 MPa
Fuel temperature	363 K
Thermodynamic conditions	
Ambient temperature	900 / 850 / 800 / 750 K
Ambient density	22.8 kg/m^3
Ambient O_2 composition	$X_{O_2} = 0.15$

($\sim$ 15 kg/m^3), TPDF models [27,28] and ESF-PDF [29] tend to predict shorter ignition delays compared to WM. Nevertheless, for flamelet-based model results reported in [30,31] the trend compared to WM results is highly dependent on the ambient thermodynamic conditions.

According to the previous discussion, this paper reports the results of a research activity focused on modeling both Spray A and Spray D spray configurations applying the RANS Unsteady Flamelet Progress Variable (UFPV) combustion model developed by the authors [20,33, 34], which is described in Section 2. The key objective of this work comprises the evaluation of the performance of this modeling approach to simulate ignition and flame structure for different nozzle sizes operating at different ambient reactivity conditions. In a first step, Spray D (reference condition) UFPV model results have been compared with those provided by a WM model to gain insight on the differences between these two modeling approaches, using the same fuel oxidation mechanism. WM has been used as a benchmark comparison of UFPV because it offers a more straightforward implementation of chemical activity within the flow, provided a reduced chemical mechanism is used. However, it fully neglects turbulence effects, which is especially critical within a RANS-type approach, and it is computationally more expensive, as results will show. Later the UFPV model analysis has been extended to include the Spray A and Spray D temperature parametric studies, gaining insight into the role of nozzle size on ignition events and quasi-steady flame structure.

2. Methodology

2.1. Target sprays' boundary conditions

As discussed in the introduction, the present study makes use of ECN hardware and standardized studies. Computations are carried-out for ECN Spray A and Spray D which correspond to single-hole nozzles with diameters of 89.4 μm (nozzle reference number 210,675) and 190.3 μm (nozzle reference number 209,135), respectively. Operating conditions under investigation are shown in Table 1, which correspond to an ambient temperature sweep at constant density and oxygen. The results presented in this study are validated using experimental data measured at CMT-Motores Térmicos in a constant-pressure vessel [2,5,6].

2.2. Computational setup

Computations have been carried-out using the CFD solver CONVERGE [35] following the traditional Lagrangian-parcel Eulerian-fluid approach. The CFD code uses a cut-cell Cartesian method for grid generation. The mesh setup schematic is shown in Fig. 1. The computational domain is a cylinder with 50 mm radius and 102 mm length for the Spray A and 140 mm for the larger Spray D. The base mesh cell size is 2 mm for both nozzle cases. A truncated cone-shaped fixed embedding is used near the nozzle region to improve accuracy around this critical zone. The fixed embedding adds 250 μm and 500 μm cells for Spray A and Spray D, respectively. In addition, adaptive mesh refinement (AMR) allows for grid resolution to be added just where needed based on velocity, temperature and fuel mass fraction gradients. As a consequence, the minimum cell size reached due to AMR is 125 μm for Spray A and 250 μm for Spray D cases. The minimum cell size for Spray A cases is the result of mesh convergence for the inert nominal condition in terms of liquid length, spray tip penetration and local mixture fraction, mixture fraction variance and axial velocity. These results are not included for the sake of brevity, but can be found in [36]. For Spray D, the minimum cell size is set based on the assumption that the flow structures can be scaled by the ratio of change in nozzle diameter.

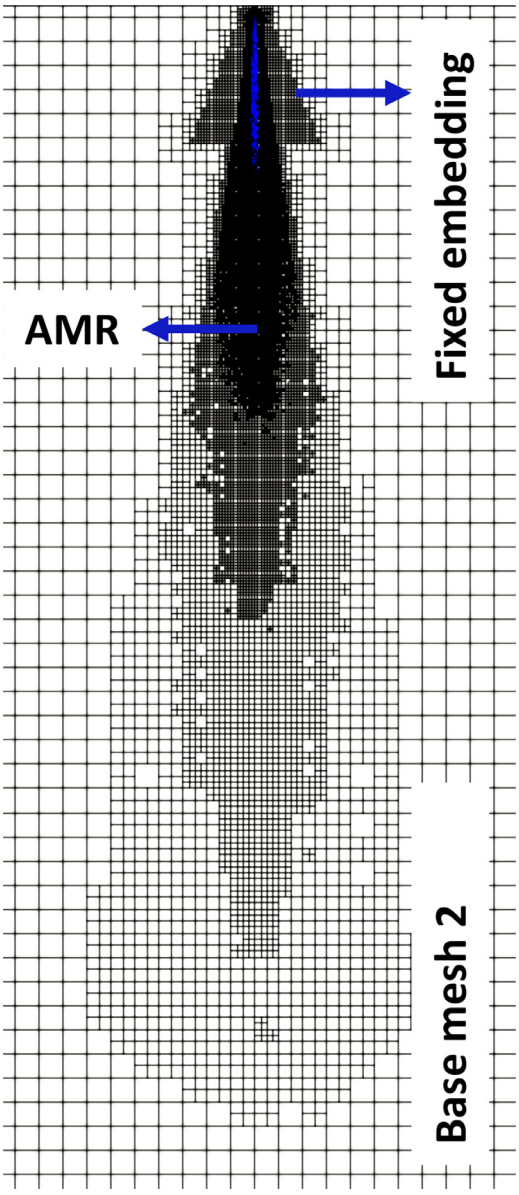

Fig. 1. Mesh setup schematic. Near nozzle fixed embedding and changes in cell size due to AMR are highlighted with blue arrows. (For interpretation of the references to color in this figure legend, the reader is referred to the web version of this article.)

The Eulerian fluid description is based on the Favre-averaged Navier–Stokes equations solved within a RANS framework. The standard $\kappa - \varepsilon$ model is used with $C_{\varepsilon 1} = 1.55$ to account for round jet correction [37,38]. On the other hand, the liquid-phase is described using the Lagrangian-parcel approach in conjunction with sub-models for droplet breakup, collisions, drag, and evaporation. The Kelvin-Helmholtz (KH) and the Rayleigh-Taylor (RT) models are used for the estimation of droplet breakup. Droplet collisions are accounted for by the no time

counter (NTC) model. Droplet drag is predicted with a model that considers variations in the drop shape using a distortion parameter. Lastly, the droplet radius rate of change due to evaporation is estimated based on the Frossling correlation [39].

The combustion modeling approach is fully discussed in [34], so only a brief summary is provided here. A skeletal mechanism with 54 species and 269 reactions [40] has been used, which has been extensively within ECN studies [12,20,21,26,34]. As for turbulence-chemistry interaction, two approaches are compared. On the one hand, the well-mixed SAGE solver (hereafter WM), which assumes that the source terms of species equations are only based on chemical kinetic rate terms calculated in terms of mean local variables. To speed up the detailed chemistry calculation, a multizone approach is used with a temperature bin size of 5 K and an equivalence ratio bin size of 0.01. On the other hand, the UFPV model by the authors [20,33] which leverages on detailed laminar flamelet calculation carried out with the flamelet solver described in [33]. This tabulated flamelet modeling approach speeds up the CFD simulation since the mixing and chemistry states are tabulated *a priori* in terms of flamelet intrinsic (i.e. control) variables, namely mixture fraction (Z) and stoichiometric scalar dissipation rate (χ_{st}), together with the so-called progress variable (Y_c). Progress variable is used to describe the transition of the mixture from inert to fully burned state as function of a linear combination of species. In this work the progress variable is defined according to

$$Y_c = 0.75Y_{CO} + Y_{CO_2} + Y_{H_2O}$$

UFPV accounts for sub-grid turbulence influence on combustion by means of a so-called presumed PDF approach, implemented on the laminar flamelet solution as a post-processing step, which integrates fluctuations of the control variables by fixed mathematical functions. In the present work, a beta-PDF and a log-normal are used for the mixture fraction and scalar dissipation rate, respectively. Fluctuation amplitude in both PDF functions are accounted for in terms of a mixture fraction variance ($\widetilde{Z''^2}$) and a constant factor $\sigma = \sqrt{2}$, respectively. This implies that the stored table or manifold for any mean variable $\tilde{\psi}$ can be expressed as a function of the mean values of the previous control variables and S, i.e. $\tilde{\psi} = \tilde{\psi}(\tilde{Z}, S, \widetilde{\chi_{st}}, \widetilde{Y_c})$, where S is the so-called segregation factor calculated as $S = \widetilde{Z''^2}/(\tilde{Z}(1-\tilde{Z}))$. In practical terms, mean species mass fraction and mean progress variable source terms $\tilde{Y}_k^{tab}(\tilde{Z}, S, \widetilde{\chi_{st}}, \widetilde{Y_c})$ and $\widetilde{\dot{\omega}Y_c}^{tab}(\tilde{Z}, S, \widetilde{\chi_{st}}, \widetilde{Y_c})$ are stored in tables with 41 points for $\tilde{Z}$, 17 points for S, 27 points for $\widetilde{\chi_{st}}$ and 51 points for $\widetilde{Y_c}$.

Coupling of the UFPV model within the CFD framework is achieved through the chemical source term of the species transport equation ($\dot{\omega}_k$) via a user defined function in CONVERGE. First, the local value of the progress variable at the cell has to be advanced by means of a simple time integration according to Eq. (1).

$$\tilde{Y}_c(t+\Delta t) = \tilde{Y}_c(t) + \widetilde{\dot{\omega}}Y_c\left(\tilde{Z}, S, \widetilde{\chi_{st}}, \tilde{Y}_c(t)\right)\Delta t \tag{1}$$

Once this is done, the average composition value from each species at the new reaction state $\tilde{Y}_k^{tab}(\tilde{Z}, S, \widetilde{\chi_{st}}, \tilde{Y}_c(t+\Delta t))$ can be retrieved from the table, from which the source term of every CFD species transport equation is evaluated through Eq. (2).

$$\widetilde{\dot{\omega}}_k = \frac{\tilde{Y}_k^{tab}\left(\tilde{Z}, S, \widetilde{\chi_{st}}, \tilde{Y}_c(t+\Delta t)\right) - \tilde{Y}_k^{cell}(t)}{\Delta t} \tag{2}$$

3. Results and discussion

As described in the introduction, the paper is focused on the application of the modeling approach to both Spray A and Spray D cases. The results section starts with the analysis of the reference condition for both nozzles, with a detailed comparison between WM and UFPV combustion approaches. After that, the sensitivity of simulation results to ambient temperature is assessed by means of the UFPV approach.

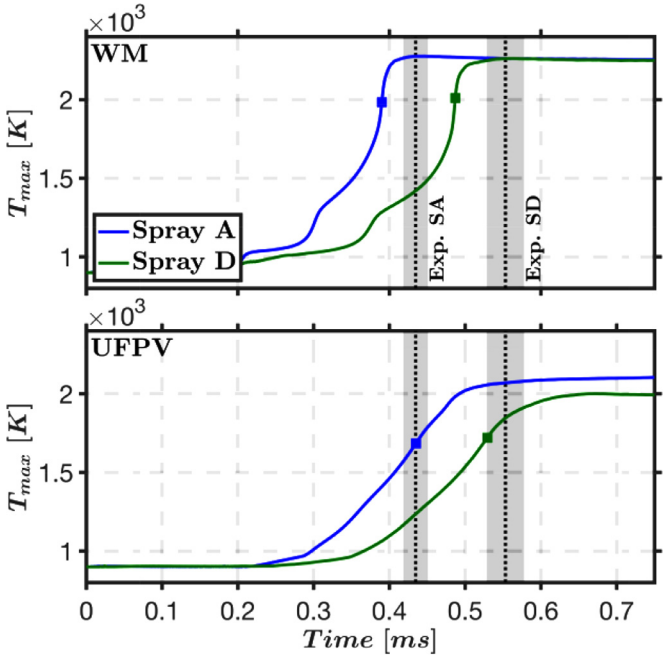

Fig. 2. Maximum temperature for Spray A (blue) and Spray D (green) using the WM (top panel) and UFPV (bottom panel) models. Square markers and dashed lines at ignition delay time for simulations and experiments, respectively. The gray shadow marks one standard deviation. Experimental results for Spray A from [5] and Spray D from [6]. (For interpretation of the references to color in this figure legend, the reader is referred to the web version of this article.)

3.1. Analysis of the reference condition

A detailed analysis of ignition and flame stabilization sequence is presented in this section using the previously described CFD modeling approach. According to ECN standards ignition delay is defined by the interval from start of injection to the timing at which the dT_{max}/dt is maximum, with T_{max} being the maximum temperature in the domain. Fig. 2 shows the time-evolution of T_{max} and the corresponding ignition delay timings. Both WM and UFPV approaches are able to predict the retarding effect of increased nozzle diameter on ignition delay. This figure also shows better agreement for UFPV predictions compared to experimental results. As a result of the turbulent integration, the UFPV approach exhibits a smoother temperature increase compared to the WM, where the two-step ignition process is much more evident.

The temporal and spatial evolution during the autoignition sequence of Spray D is provided in Fig. 3, where local heat release rate (HRR) is plotted in the upper half of the spray images. The lower half shows formaldehyde (CH_2O) and hydroxyl radical (OH) contours, which are considered as low- and high-temperature ignition tracers [41,42], respectively. Low-temperature heat release (HR) is initiated at spray edge and propagates towards the spray core, followed by high-temperature ignition occurring at the stoichiometric radius for both models. Compared to Spray A [34] and also in agreement with experiments [6], Spray D ignition happens clearly upstream of the spray tip, while in the smaller nozzle high-temperature ignition for the same operating conditions occurs at the head vortex region. The UFPV model shows a more spatially distributed (volumetric) ignition sequence, due to the presumed-PDF integration [34], which also explains the smoother HRR seen in the last row of Fig. 3 and peak temperature evolution in Fig. 2. The integrated amount of OH and CH_2O is similar for both WM and UFPV, although there is a broader distribution of CH_2O preceding to high-temperature ignition for UFPV.

The reacting spray shows a quasi-steady appearance shortly after the ignition sequence, which extends until the end of injection. This quasi-

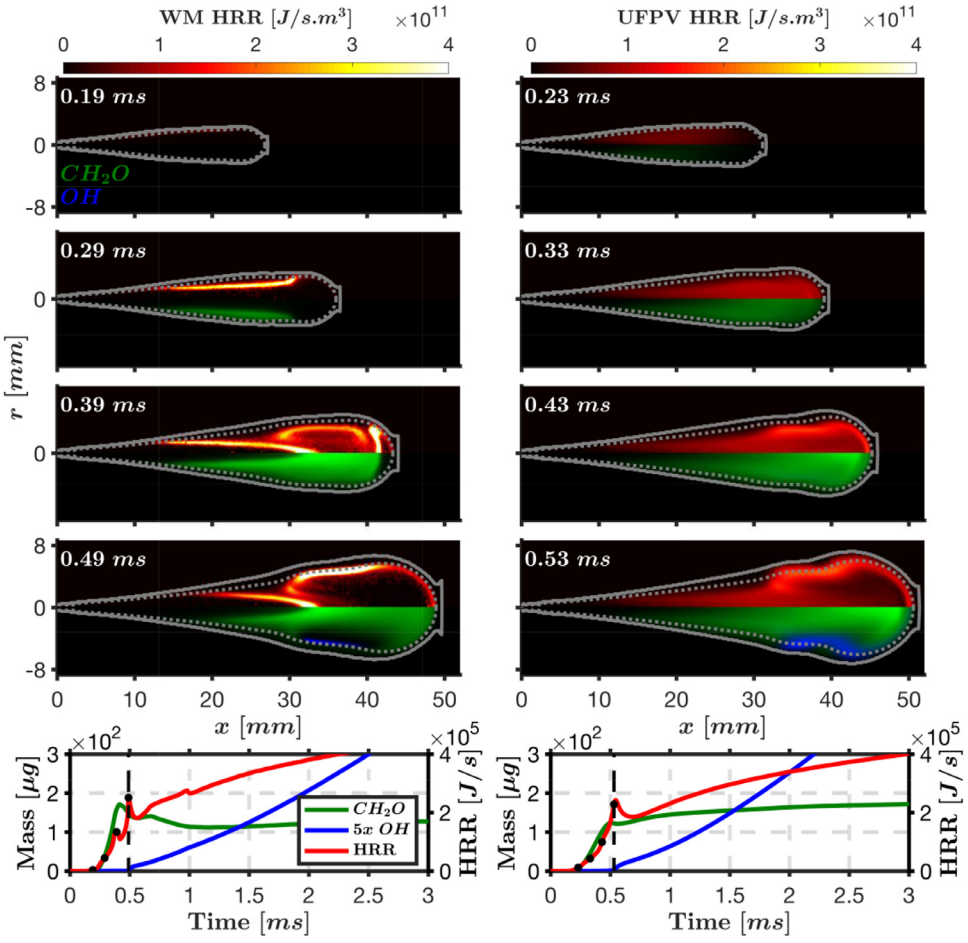

Fig. 3. Autoignition sequence for Spray D using the WM (left panels) and UFPV (right panels) combustion models. In each panel, local heat release rate (top half) and false color images (bottom half) are shown. Color scale for heat release rate is shown at the top, while color scale for species has been normalized for each frame. Spray radius and stoichiometric mixture fraction isocontour marked with solid and dotted lines, respectively. Integrated heat release rate and species mass is shown at bottom panels.

steady layout is analyzed at 4.45 ms in Fig. 4 by means of key species contours. The flame structure shows a low-temperature region upstream the lift-off, indicated by CH_2O, while the diffusion flame front, is located around the stoichiometric surface, as indicated by the presence of OH radical. Rich combustion products, such as acetylene (C_2H_2) appear within the spray core. Despite the similar flame structure provided by both models, shorter, and closer to measurements, lift-off flame is predicted by UFPV [34].

The lower part of the Figure shows a 'transverse integrated mass' for the key species, which is defined at each axial coordinate as in Eq. (3):

$$TIM_k(x) = \int_{r=0}^{R} p(x,r) \cdot Y_K(x,r) \cdot 2\pi r \cdot dr \tag{3}$$

This variable makes it possible to compare the axial distribution of the different species. The figure clearly shows that, within the quasi-steady state, chemical activity starts closer to the nozzle with the low temperature reactions, namely CH_2O, increasing with axial distance until reaching the lift-off location (roughly 38 mm for the WM and 26 mm for the UFPV), which denotes the start of the high-temperature reactions. At this point formaldehyde curve levels off and starts dropping with axial distance, and OH and C_2H_2 start rising. OH seems to follow a quite steady evolution with a slight increase with axial distance, while C_2H_2 tends to reach a peak at around 100 mm from the nozzle. Values at the tip end of the axial extent (from 120 mm) are already affected by the transient spray head, so evolution departs from the quasi-steady one.

A higher degree of spatial overlapping of the key species is observed for the flamelet-based approach. This is quite clear in the case of CH_2O, which shows a sharp drop at around 35 mm after the leveling-off for the WM evolution, coincident with a small peak in OH. For the UFPV case a much milder leveling-off and later drop after 45 mm is observed for CH_2O. Given the similar values of OH and C_2H_2 along the main flame length for both TCI approaches, it is quite clear that the main effect of the TCI occurs around the lift-off length location.

3.2. The effect of ambient temperature

The analysis carried out for the nominal conditions is extended throughout this section for Spray A and Spray D at different ambient temperatures ranging from 750 to 900 K using the UFPV combustion model. Results are validated in terms of spray tip penetration, ignition delay time and lift-off length, after which the flame structure at ignition timing and quasi-steady state is presented.

3.2.1. Spray tip penetration and global combustion indicators

In order to assess the predictability of the computational setup in relation to the reacting spray dynamics, Fig. 5 shows results for the spray tip penetration and time-resolved lift-off length. For validation purposes, experimental results for spray tip penetration are also plotted (black line) with the 95% confidence interval (gray shadow) for Spray A at the whole range of ambient temperatures studied and for Spray D at 800 and 900 K. No experimental tip penetration data are available for this nozzle at the lowest and intermediate temperatures, and the same applies to time-resolved lift-off length. Regardless the ambient temperature value, the larger nozzle exhibits faster penetration as a consequence of the increased momentum flux in comparison to the smaller nozzle. Aside from the momentum flux, detailed studies in [3] have shown that reacting tip penetration is the result of flow acceleration and the radial expansion of the jet occurring at the ignition timing, both effects as a

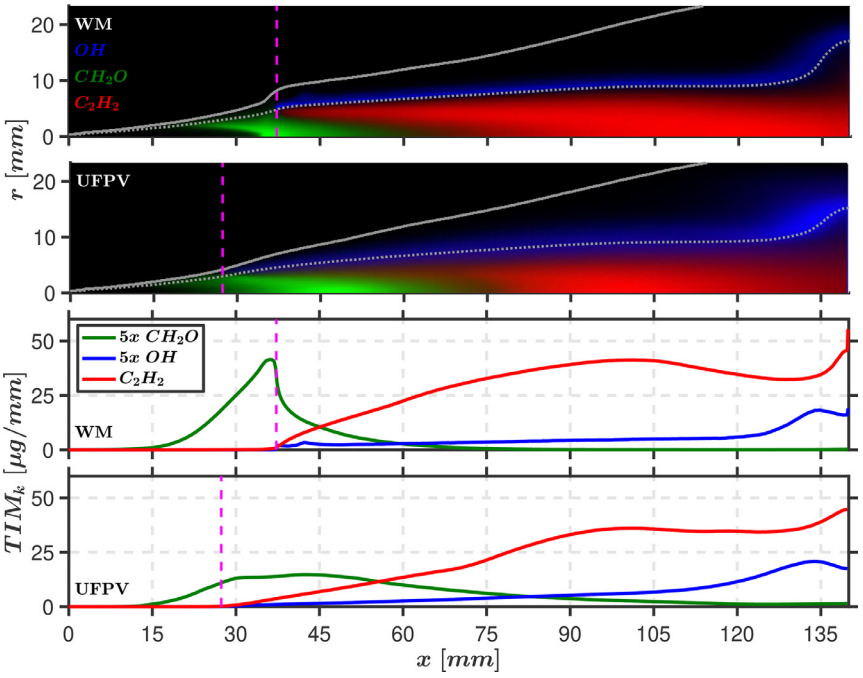

Fig. 4. False color images and transverse integrated mass of key species for Spray D using the WM (first and third panels) and UFPV (second and fourth panels) combustion models. Spray radius, stoichiometric mixture fraction isocontour and lift-off length marked with solid, dotted and dashed lines, respectively.

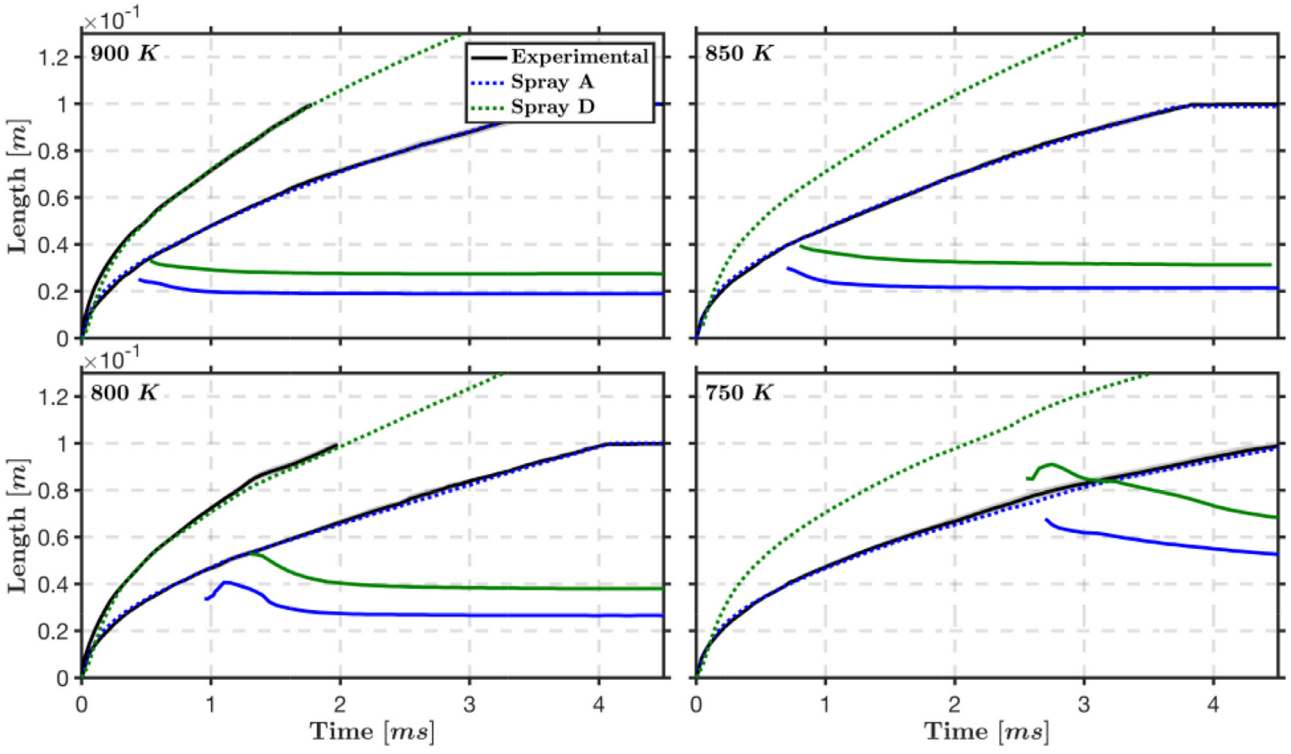

Fig. 5. Spray tip penetration (dotted line) and lift-off length (solid line) for Spray A (blue) and Spray D (green) at different ambient temperatures. The gray shadow marks the 95% confidence interval for the experimental data. Experimental data for Spray A from [2] and Spray D from [6]. (For interpretation of the references to color in this figure legend, the reader is referred to the web version of this article.)

result of the density drop during the inert to reacting transition. For all cases where experimental data are available, both Spray A and Spray D numerical results show that the computational setup used successfully reproduces the experimental tip penetration values. Additionally, local mixture fraction, mixture fraction variance and axial velocity under inert conditions were already validated in a previous work [34] showing that the local flow state is adequately reproduced by the model. Time-resolved lift-off length results show that the flame stabilizes further downstream from the nozzle for Spray D in comparison to Spray A for all temperature conditions. Both nozzles reach a quasi-steady state for any ambient temperature, as depicted by the flat lift-off length evolution, with the exception of 750 K, where lift-off length is clearly receding with time after the longest ignition delay period. This behavior is observed for both nozzles.

Combustion global indicators are also validated against experimental data in Fig. 6. As described in Section 3.1 and following ECN standards,

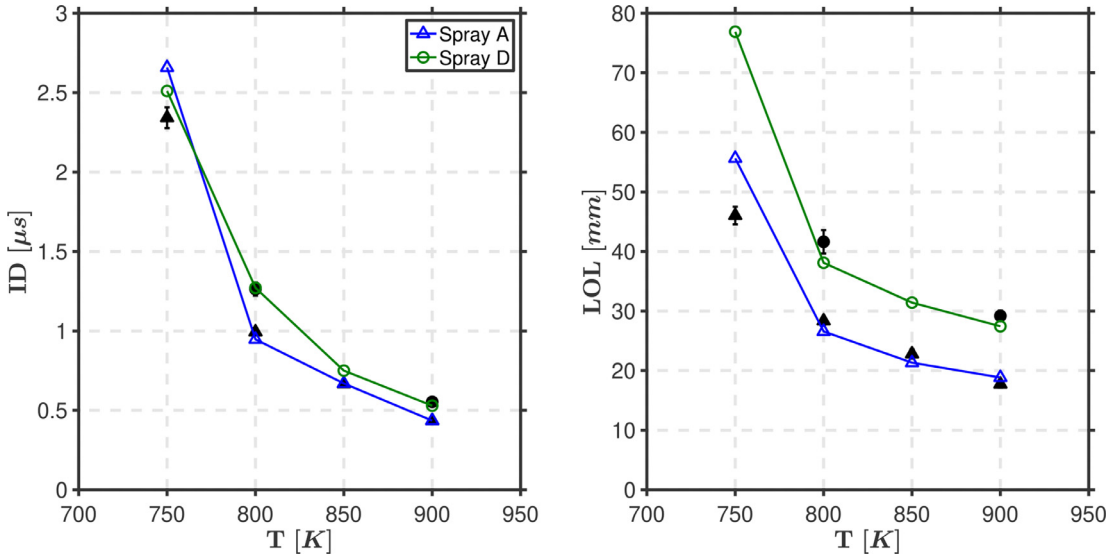

Fig. 6. Ignition delay time for Spray A (blue) and Spray D (green) at different ambient temperatures. Vertical bars mark one standard deviation for the experimental data. Experimental data for Spray A from [5] and Spray D from [6]. (For interpretation of the references to color in this figure legend, the reader is referred to the web version of this article.)

ignition delay time is based on the temporal derivative of maximum temperature. For the lift-off length, the criteria used is based on the location at which 14% of the maximum OH mass fraction is reached. This location is tracked at each time in the simulation after the ignition (Fig. 5) and is time-averaged once it has stabilized. There is an exception for the 750 K case (both Spray A and Spray D) for which the time-resolved lift-off length doesn't stabilize by the end of the injection and the values reported in Fig. 6 correspond to the value at that time.

Both ignition delay and lift-off length are in excellent agreement in the range of 800 to 900 K. The trend of slightly longer ignition delay and longer lift-off length for the larger nozzle is captured by the model. At the lowest temperature condition, at which there is only experimental data for Spray A, the two global combustion indicators are over-predicted. Nonetheless, the level of agreement is still satisfactory keeping in mind that this low-temperature condition is challenging both numerically and experimentally. On the one hand, even with a long injection (5 ms for Spray A and 4.5 ms for Spray D), the spray has not reached quasi steady state yet (evidenced in time-resolved lift-off length results in Fig. 5) [20]. On the other hand, experimental measurements are also challenging, as autoignition takes place further away from the nozzle and closer to the field-of-view limit.

3.2.2. Flame structure at ignition timing and quasi-steady state

In this section, the effect of ambient temperature on the flame structure is analyzed for the two nozzles under study at the time of ignition and at quasi-steady state. Fig. 7 shows the results at the time of ignition for Spray A (left panels) and Spray D (right panels) using the same layout as in Fig. 3 with the local heat release rate at the top half and key species false color images at the bottom half. To facilitate the comparison among the two nozzles, spatial coordinates have been normalized by an equivalent diameter estimated according to $d_{eq} = d_{effective}\sqrt{\rho_{fuel}/\rho_{air}}$. Through this normalization, differences in air entrainment due to the nozzle size are taken into account [43] leading to the same mixture fraction for either nozzle at the same normalized spatial coordinates.

From top to bottom in Fig. 7, the ambient temperature decreases, and the ignition locations shifts further away from the nozzle towards leaner mixtures. For all cases, the location of ignition is characterized by an intense heat release rate spot, the appearance of OH and the consequent consumption of CH_2O. In the range of 800–900 K, the ignition location for Spray A tends to be closer to the spray head, in contrast to Spray D for which ignitions seems to take place radially displaced in a wider zone of the spray. This feature has been reported experimentally for the nominal ambient temperature condition [38] and can be explained by less strained mixtures and longer residence time in the larger nozzle, which facilitates autoignition in this radially displaced location as reported by the authors in [34]. At 750 K ignition takes place at the spray head for both nozzles, although the relative differences in location still holds valid i.e., Spray A ignition location downstream (in normalized coordinates) from that of Spray D. In fact, this difference in location in normalized coordinates at ignition can be extended for the whole range of ambient temperatures, and shows that at the same ambient temperature, the smaller nozzle with a consequent faster mixing process ignites at leaner mixtures compared to the larger Spray D.

Differences observed for the ignition location in Fig. 7, in terms of mixing among the nozzles and ambient temperatures, remain consistent for the lift-off length location at quasi-steady state as reported in Fig. 8. For both nozzles, lift-off length stabilizes further away from the nozzle as the ambient temperature is decreased. Similarly, for the same ambient temperature the lift-off length normalized by the equivalent diameter stabilizes at a farther location for spray A in relation to Spray D showing the tendency for the larger nozzle to burn under more fuel rich conditions.

In addition to lift-off length results, the false color images plotted in Fig. 8 allow to evaluate the flame structure for key species. For all ambient temperature values, CH_2O, OH and C_2H_2 can be found at the base of the flame, around the stoichiometric mixture fraction isocontour and at the spray core, respectively, in accordance with the description made for the reference condition (see Fig. 4). The flame structure around the lift-off location does not change essentially with decreasing ambient temperature, it is mainly shifted to positions further away from the nozzle. Despite evident similarities in relation to species location, it is worth noting that the peak C_2H_2 mass fraction changes in accordance to changes in LOL, with an increasing value as the flame is stabilized at richer mixtures as a consequence of higher ambient temperatures and/or bigger nozzle diameter. For instance, peak C_2H_2 mass fraction (reported at the top left corner for each case in Fig. 8) decreases by a factor of 1.3 at 900 K by changing the nozzle diameter from Spray D to Spray A, while for the large nozzle it drops by a factor of 1.05 if the ambient temperature drops from 900 to 850 K. These changes in LOL and peak C_2H_2 mass fraction hint at potentially more soot formation for the bigger nozzle and higher temperatures, since C_2H_2 is the main building-block for the formation and growth of polycyclic aromatic hydrocarbon and consequently soot [44,45]. Lastly, it is also worth mentioning that the 750 K cases have not fully reached the quasi-steady state by the end of

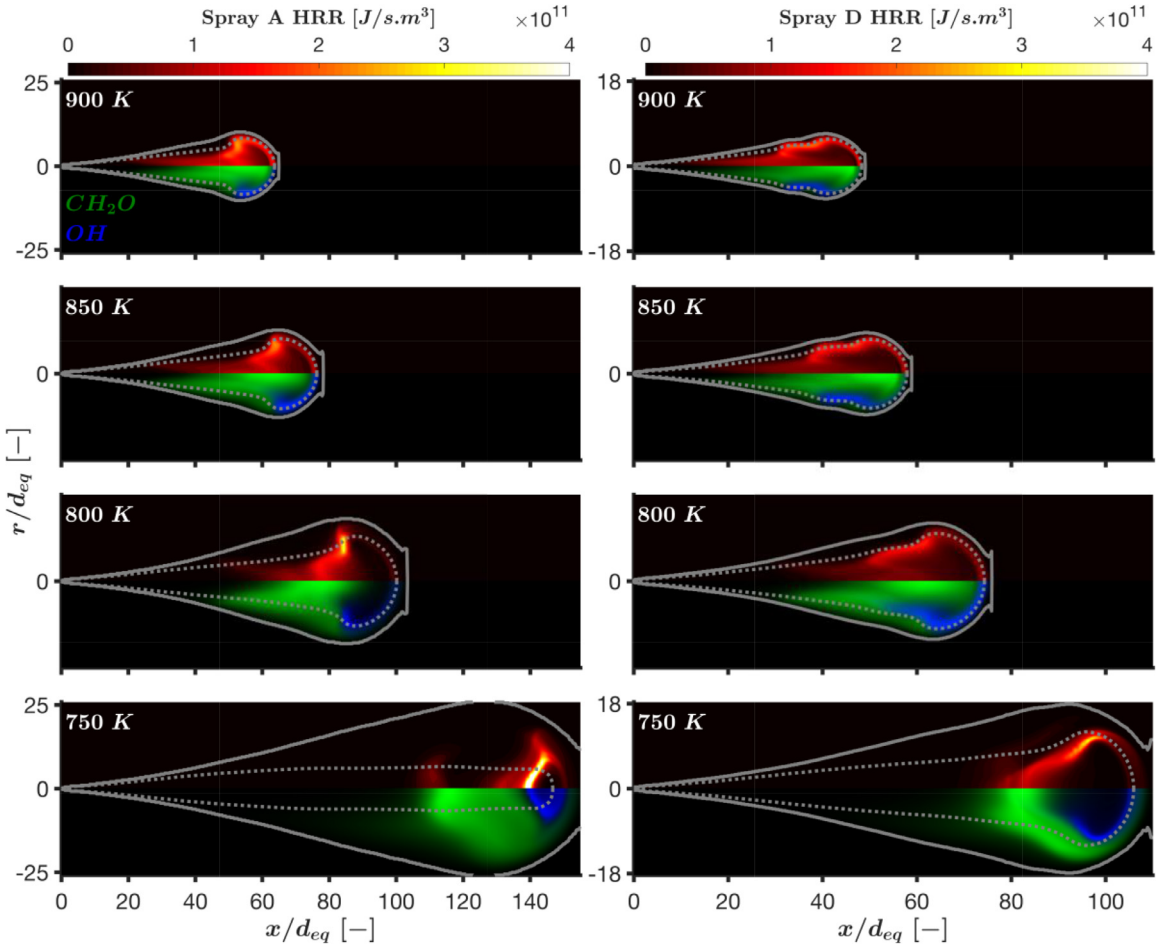

Fig. 7. Local heat release rate (top half) and key species false color images (bottom half) at ignition timing for Spray A (left panels) and Spray D (right panels) at different ambient temperatures. Spray radius and stoichiometric mixture fraction isocontour marked with solid and dotted lines, respectively.

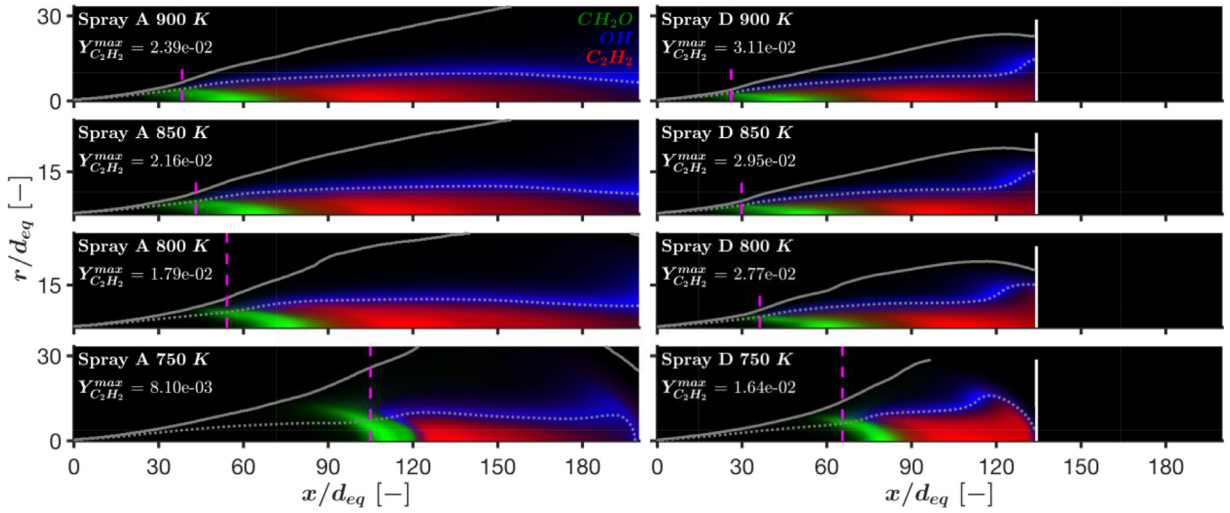

Fig. 8. Key species false color images for Spray A (left panels) and Spray D (right panels). Spray radius, stoichiometric mixture fraction isocontour and lift-off length marked with solid, dotted and dashed lines, respectively. A white vertical line marks the end of the computational domain for Spray D cases.

the injection as evidenced by the flame structure depicted in the bottom panes (see Fig. 8). For the lowest ambient temperature condition, both Spray A and Spray D exhibit a CH_2O structure that is still transitioning into the longer curved shape observed for the rest of cases, while lift-off length is not stabilized yet and still shifting upstream in relation to the ignition location, as shown in Fig. 5.

4. Summary and conclusions

The combustion process from the ECN Spray A and Spray D has been analyzed based on CFD results. For the analysis of the Spray D reference condition at 900 K, the well-mixed (WM model) and the flamelet (UFPV model) sub-grid assumptions have been assessed in relation to

the autoignition sequence and flame structure at quasi-steady state. After that, the analysis of UFPV results has been extended for both Spray A and Spray D at various ambient temperature boundary conditions. Main findings can be summarized as follows:

- UFPV delivers a more accurate prediction of global combustion indicators for both nozzles. This has been shown at the reference temperature case, but the conclusion extends to other operating conditions not shown in the present study. This indicates that, compared to the simple WM approach, a more refined TCI model is needed to successfully predict combustion in this type of sprays with a RANS-type simulation.
- The use of the UFPV model also considerably reduces the computational cost of the simulations. Much of the computational time saving comes from solving the chemistry in advance and decoupling it from the fluid dynamics solution, in contrast to the on-line detailed chemistry solver from the WM model. The cost of a WM model simulation is in the order of $50.8x10^3$ core hours and it is in the order of $1.2x10^3$ core hours for the UFPV model.
- For the reference Spray D condition, WM and UFPV model results show a similar autoignition sequence mainly characterized by a cool flame wave moving from the spray radial periphery towards the spray core. At the time of ignition, CH_2O produced during the cool flame period is consumed as OH appears at the ignition spot located in the spray radial periphery.
- At quasi-steady state, WM and UFPV models also predict a similar flame structure for the reference Spray D case. In the results from both combustion models, CH_2O can be found at the base of the flame, OH around the stoichiometric mixture fraction isocontour and C_2H_2 at the spray core. The biggest differences between both modeling approaches are related to local details, with well delimited zones in WM model in contrast to some degree of overlapping between species in UFPV model results as a result of turbulent averaging.
- At the different ambient temperatures, predicted spray tip penetration, ignition delay and lift-off length simulation results are in good agreement with experimental data for both nozzle sizes. The flame structure at the time of ignition shows that at the same ambient temperature, the ignition location for Spray D takes place at richer mixtures compared to Spray A. This holds over all tested ambient temperature values. This observation can also be extended to the quasi-steady state, at which the lift-off length for Spray D also stabilizes at richer mixtures compared to the smaller nozzle, which justifies the more important soot formation in the larger nozzle.

Declaration of Competing Interest

The authors declare that they have no known competing financial interests or personal relationships that could have appeared to influence the work reported in this paper.

Acknowledgments

This work was partially funded by the Government of Spain through the CHEST Project (TRA2017-89139-C2-1-R). CONVERGENT SCIENCE Inc support is greatly acknowledged. The authors also want to express their gratitude to Dr. Bertrand Naud from CIEMAT for the development of the flamelet solver used in this work.

References

[1] Engine Combustion Network, (2020). https://ecn.sandia.gov/.
[2] J.V. Pastor, R. Payri, J.M. Garcia-Oliver, J.-.G. Nerva, Schlieren measurements of the ECN-spray A penetration under inert and reacting conditions, in: SAE Technical Paper 2012-01.0456, 2012, doi:10.4271/2012-01-0456.
[3] J.M. Desantes, J.M. García-Oliver, T. Xuan, W. Vera-Tudela, A study on tip penetration velocity and radial expansion of reacting diesel sprays with different fuels, Fuel 207 (2017) 323–335, doi:10.1016/j.fuel.2017.06.108.
[4] L.M. Pickett, J. Manin, C.L. Genzale, D.L. Siebers, M.P.B. Musculus, C.A. Idicheria, Relationship between diesel fuel spray vapor penetration/dispersion and local fuel mixture fraction, SAE Int. J. Engines 4 (2011) 764–799, doi:10.4271/2011-01-0686.
[5] J. Benajes, R. Payri, M. Bardi, P. Martí-Aldaraví, Experimental characterization of diesel ignition and lift-off length using a single-hole ECN injector, Appl. Therm. Eng. 58 (2013) 554–563, doi:10.1016/j.applthermaleng.2013.04.044.
[6] J.V. Pastor, J.M. Garcia-Oliver, A. Garcia, A. Morales López, An experimental investigation on spray mixing and combustion characteristics for spray C/D nozzles in a constant pressure vessel, in: Proceedings of the International Powertrains Fuels and Lubricants Meeting, 2018, doi:10.4271/2018-01-1783.
[7] J.M. García-Oliver, L.-.M. Malbec, H.B. Toda, G. Bruneaux, A study on the interaction between local flow and flame structure for mixing-controlled diesel sprays, Combust. Flame 179 (2017) 157–171, doi:10.1016/j.combustflame.2017.01.023.
[8] S.A. Skeen, J. Manin, L.M. Pickett, E. Cenker, G. Bruneaux, K. Kondo, T. Aizawa, F. Westlye, K. Dalen, A. Ivarsson, T. Xuan, J.M. Garcia-Oliver, Y. Pei, S. Som, W. Hu, R.D. Reitz, T. Lucchini, G. D'Errico, D. Farrace, S.S. Pandurangi, Y.M. Wright, M.A. Chishty, M. Bolla, E. Hawkes, A progress review on soot experiments and modeling in the engine combustion network (ECN), SAE Int. J. Engines 9 (2016) 883–898, doi:10.4271/2016-01-0734.
[9] T. Xuan, J.M. Desantes, J.V. Pastor, J.M. Garcia-Oliver, Soot temperature characterization of spray a flames by combined extinction and radiation methodology, Combust. Flame 204 (2019) 290–303, doi:10.1016/j.combustflame.2019.03.023.
[10] F.R. Westlye, M. Battistoni, S.A. Skeen, J. Manin, L.M. Pickett, A. Ivarsson, Penetration and combustion characterization of cavitating and non-cavitating fuel injectors under diesel engine conditions, in: Proceedings of the SAE World Congress and Exhibition, 2016, doi:10.4271/2016-01-0860.
[11] N. Maes, S.A. Skeen, M. Bardi, R.P. Fitzgerald, L.-.M. Malbec, G. Bruneaux, L.M. Pickett, K. Yasutomi, G. Martin, Spray penetration, combustion, and soot formation characteristics of the ECN spray C and spray D injectors in multiple combustion facilities, Appl. Therm. Eng. 172 (2020) 115136, doi:10.1016/j.applthermaleng.2020.115136.
[12] L. Zhao, Y. Pei, Y. Zhang, M.L. Traver, M.M. Ameen, Spray characteristics evaluation on three different ECN single-hole injectors under compression ignition engine conditions, in: Proceedings of the ILASS-Americas 31st Annual Conference on Liquid Atomization and Spray Systems, Madison, WI, 2020.
[13] M. Ihme, P.C. Ma, L. Bravo, Large eddy simulations of diesel-fuel injection and auto-ignition at transcritical conditions, Int. J. Engine Res. 20 (2019) 58–68, doi:10.1177/1468087418819546.
[14] Z. Yue, R.D. Reitz, An equilibrium phase spray model for high-pressure fuel injection and engine combustion simulations, Int. J. Engine Res. 20 (2017) 203–215, doi:10.1177/1468087417744144.
[15] H. Wang, Y. Ra, M. Jia, R.D. Reitz, Development of a reduced n -dodecane-PAH mechanism and its application for n -dodecane soot predictions, Fuel 136 (2014) 25–36, doi:10.1016/j.fuel.2014.07.028.
[16] Y. Pei, S. Som, E. Pomraning, P.K. Senecal, S.A. Skeen, J. Manin, L.M. Pickett, Large eddy simulation of a reacting spray flame with multiple realizations under compression ignition engine conditions, Combust. Flame 162 (2015) 4442–4455, doi:10.1016/j.combustflame.2015.08.010.
[17] O. Owoyele, P. Kundu, M.M. Ameen, T. Echekki, S. Som, Application of deep artificial neural networks to multi-dimensional flamelet libraries and spray flames, Int. J. Engine Res. (2019), doi:10.1177/1468087419837770.
[18] D. Aubagnac-Karkar, J.-.B. Michel, O. Colin, N. Darabiha, Combustion and soot modelling of a high-pressure and high-temperature dodecane spray, Int. J. Engine Res. 19 (2018) 434–448, doi:10.1177/1468087417714351.
[19] P. Kundu, M.M. Ameen, C. Xu, U. Unnikrishnan, T. Lu, S. Som, Implementation of detailed chemistry mechanisms in engine simulations, J. Eng. Gas Turbines Power (2018) 141, doi:10.1115/1.4041281.
[20] J.M. Desantes, J.M. García-Oliver, R. Novella, E.J. Pérez-Sánchez, Application of an unsteady flamelet model in a RANS framework for spray A simulation, Appl. Therm. Eng. 117 (2017) 50–64, doi:10.1016/j.applthermaleng.2017.01.101.
[21] J.M. Desantes, J.M. García-Oliver, R. Novella, E.J. Pérez-Sánchez, Application of a flamelet-based CFD combustion model to the LES simulation of a diesel-like reacting spray, Comput. Fluids 200 (2020) 104419, doi:10.1016/j.compfluid.2019.104419.
[22] T. Lucchini, G. D'Errico, A. Onorati, A. Frassoldati, A. Stagni, G. Hardy, Modeling non-premixed combustion using tabulated kinetics and different flame structure assumptions, SAE Int. J. Engines 10 (2017) 593–607.
[23] H. Kahila, A. Wehrfritz, O. Kaario, M. Ghaderi Masouleh, N. Maes, B. Somers, V. Vuorinen, Large-eddy simulation on the influence of injection pressure in reacting spray A, Combust. Flame 191 (2018) 142–159, doi:10.1016/j.combustflame.2018.01.004.
[24] S.S. Pandurangi, M. Bolla, Y.M. Wright, K. Boulouchos, S.A. Skeen, J. Manin, L.M. Pickett, Onset and progression of soot in high-pressure n-dodecane sprays under diesel engine conditions, Int. J. Engine Res. 18 (2017) 436–452, doi:10.1177/1468087416661041.
[25] M. Bolla, M.A. Chishty, E.R. Hawkes, Q.N. Chan, S. Kook, Influence of turbulent fluctuations on radiation heat transfer, NO and soot formation under ECN spray A conditions, Proc. Combust. Inst. 36 (2017) 3551–3558, doi:10.1016/j.proci.2016.06.173.
[26] M.A. Chishty, M. Bolla, E.R. Hawkes, Y. Pei, S. Kook, Soot formation modelling for n-dodecane sprays using the transported PDF model, Combust. Flame 192 (2018) 101–119, doi:10.1016/j.combustflame.2018.01.028.
[27] S. Bhattacharjee, D.C. Haworth, Simulations of transient n-heptane and n-dodecane spray flames under engine-relevant conditions using a transported PDF method, Combust. Flame 160 (2013) 2083–2102, doi:10.1016/j.combustflame.2013.05.003.
[28] Y. Pei, E.R. Hawkes, S. Kook, Transported probability density function modelling of the vapour phase of an n-heptane jet at diesel engine conditions, Proc. Combust. Inst. 34 (2013) 3039–3047, doi:10.1016/j.proci.2012.07.033.

[29] K.M. Pang, M. Jangi, X.-S. Bai, J. Schramm, J.H. Walther, Modelling of diesel spray flames under engine-like conditions using an accelerated Eulerian stochastic field method, Combust. Flame 193 (2018) 363–383, doi:10.1016/j.combustflame.2018.03.030.
[30] G. D'Errico, T. Lucchini, F. Contino, M. Jangi, X.-S. Bai, Comparison of well-mixed and multiple representative interactive flamelet approaches for diesel spray combustion modelling, Combust. Theory Model. 18 (2014) 65–88, doi:10.1080/13647830.2013.860238.
[31] A. Kosters, A. Karlsson, M. Oevermann, G. D'Errico, T. Lucchini, RANS predictions of flame lift-off: comparison of a reactor and a flamelet combustion model to the well stirred approach, Combust. Theory Model 25 (2015) 81–106.
[32] T. Lucchini, G. D'Errico, T. Cerri, A. Onorati, G. Hardy, Experimental validation of combustion models for diesel engines based on tabulated kinetics in a wide range of operating conditions, in: Proceedings of the 13th International Conference on Engines and Vehicles, 2017, doi:10.4271/2017-24-0029.
[33] B. Naud, R. Novella, J.M. Pastor, J.F. Winklinger, RANS modelling of a lifted H 2/N 2 flame using an unsteady flamelet progress variable approach with presumed PDF, Combust. Flame 162 (2015) 893–906, doi:10.1016/j.combustflame.2014.09.014.
[34] J.M. Desantes, J.M. Garcia-Oliver, R. Novella, L. Pachano, A numerical study of the effect of nozzle diameter on diesel combustion ignition and flame stabilization, Int. J. Engine Res. 21 (2020) 101–121, doi:10.1177/1468087419864203.
[35] CONVERGE CFD Software, (n.d.). https://convergecfd.com.
[36] L. Pachano, CFD Modeling of Combustion and Soot Production in Diesel Sprays, Universitat Politècnica de València, 2020.
[37] S.B. POPE, An explanation of the turbulent round-jet/plane-jet anomaly, AIAA J. 16 (1978) 279–281, doi:10.2514/3.7521.
[38] R. Novella, A. García, J.M. Pastor, V. Domenech, The role of detailed chemical kinetics on CFD diesel spray ignition and combustion modelling, Math. Comput. Model. 54 (2011) 1706–1719, doi:10.1016/j.mcm.2010.12.048.
[39] CONVERGE manual. Madison, WI: Convergent Science, 2016.
[40] T. Yao, Y. Pei, B.-J. Zhong, S. Som, T. Lu, K.H. Luo, A compact skeletal mechanism for n -dodecane with optimized semi-global low-temperature chemistry for diesel engine simulations, Fuel 191 (2017) 339–349, doi:10.1016/j.fuel.2016.11.083.
[41] N. Maes, M. Meijer, N. Dam, B. Somers, H. Baya Toda, G. Bruneaux, S.A. Skeen, L.M. Pickett, J. Manin, Characterization of spray A flame structure for parametric variations in ECN constant-volume vessels using chemiluminescence and laser-induced fluorescence, Combust. Flame 174 (2016) 138–151, doi:10.1016/j.combustflame.2016.09.005.
[42] R.N. Dahms, G.A. Paczko, S.A. Skeen, L.M. Pickett, Understanding the ignition mechanism of high-pressure spray flames, Proc. Combust. Inst. 36 (2017) 2615–2623, doi:10.1016/j.proci.2016.08.023.
[43] F.P. Ricou, D.B. Spalding, Measurements of entrainment by axisymmetrical turbulent jets, J. Fluid Mech. 11 (1961) 21–32, doi:10.1017/S0022112061000834.
[44] Bockhorn, Soot formation in combustionMechanisms and Models, Springer- Verlag, Berlin Heidelberg, 1994.
[45] J. Warnatz, U. Maas, R.W. Dibble, Combustion, Springer, Berlin, 2006.